

Conjugate Heat Transfer Measurements and Predictions of a Blade Endwall With a Thermal Barrier Coating

Amy Mensch

Department of Mechanical and Nuclear Engineering,
The Pennsylvania State University,
University Park, PA 16802
e-mail: aem277@psu.edu

Karen A. Thole

Department of Mechanical and Nuclear Engineering,
The Pennsylvania State University,
University Park, PA 16802
e-mail: kthole@psu.edu

Brent A. Craven

Department of Mechanical and Nuclear Engineering,
The Pennsylvania State University,
University Park, PA 16802
e-mail: bac207@psu.edu

Multiple thermal protection techniques, including thermal barrier coatings (TBCs), internal cooling and external cooling, are employed for gas turbine components to reduce metal temperatures and extend component life. Understanding the interaction of these cooling methods, in particular, provides valuable information for the design stage. The current study builds upon a conjugate heat transfer model of a blade endwall to examine the impact of a TBC on the cooling performance. The experimental data with and without TBC are compared to results from conjugate computational fluid dynamics (CFD) simulations. The cases considered include internal impingement jet cooling and film cooling at different blowing ratios with and without a TBC. Experimental and computational results indicate the TBC has a profound effect, reducing scaled wall temperatures for all cases. The TBC effect is shown to be more significant than the effect of increasing blowing ratio. The computational results, which agree fairly well to the experimental results, are used to explain why the improvement with TBC increases with blowing ratio. Additionally, the computational results reveal significant temperature gradients within the endwall, and information on the flow behavior within the impingement channel. [DOI: 10.1115/1.4028233]

Introduction

The ongoing aim to increase power output in gas turbines results in increasing gas temperatures at the turbine inlet. Consequently, turbine parts must withstand thermal conditions that exceed the material allowable temperatures. For that reason cooling technologies are required to maintain part life. Coolant is extracted from the compressor and directed into turbine components. First, the coolant removes heat from internal surfaces, and then the coolant is ejected through film cooling holes providing a coolant layer on the outer surface. In addition, insulating, high temperature ceramic coatings, known as TBCs, are often applied on external surfaces to further protect the parts that are exposed to the highest thermal loads. A critical need for engineers is the ability to accurately predict the overall thermal performance of configurations which include a combination of the available cooling technologies.

The objective of this study is to evaluate the improvement in thermal performance when a TBC is applied to a typical gas turbine endwall configuration for different coolant flowrates. It is established that a TBC can provide a dramatic reduction in metal temperatures and thus has been applied in many designs [1]. Both experimental measurements and computational predictions of a scaled endwall model are used to quantify the benefit of a TBC for a fully cooled endwall. A second objective is to assess the predictions with experimental results. Once validated, the simulations provide additional insight into endwall temperatures and heat transfer that cannot be easily measured. This study builds upon the experimental work by Mensch and Thole [2] on a conjugate endwall with impingement and film cooling, to examine the thermal effects of a TBC.

Relevant Literature

There has been considerable emphasis recently on conjugate heat transfer and determining the scaled metal temperature, or overall effectiveness, of gas turbine surfaces both computationally and experimentally. Albert et al. [3] showed that it is important to model the appropriate dimensionless parameters to obtain relevant measurements in these types of studies. The critical parameters are the Biot number, Bi ; the ratio of external to internal heat transfer coefficients, h_{∞}/h_i ; the Reynolds number, Re ; and the scaled geometry. The first studies to provide measurements of conjugate heat transfer on a conducting C3X vane were by Hylton et al. [4,5] and Turner et al. [6]. The engine relevance of these data is limited because matched Bi and h_{∞}/h_i were not confirmed; however, these initial studies improved understanding of conjugate heat transfer in a vane and provided an important data set for comparison to computational work.

Endwall heat transfer can behave differently compared to a vane surface because of the presence of strong external secondary flows, namely the horseshoe and passage vortices. The passage vortices affect the endwall by skewing the direction of endwall flow and locally increasing the external heat transfer coefficients as shown by Kang and Thole [7]. The first experimental study for a conjugate endwall exposed to passage flows was completed by Mensch and Thole [2]. Although the endwall was cooled with both impingement and film cooling, the impingement had a greater influence on the scaled wall temperature. Furthermore, significant temperature gradients were observed due to the use of engine matched Bi , which is the same value as the current study. Lynch et al. [8] compared experimental and computational results for an endwall with the same blade geometry for an adiabatic wall boundary condition, as well as for a constant wall heat flux boundary condition to measure the external heat transfer coefficients.

The thermal effect of TBC on a conjugate surface was considered by Maikell et al. [9] in an experimental leading edge model with a Bi of 1–2.1, matched to an engine leading edge. The TBC case had cooler leading edge wall temperatures but hotter external

Contributed by the International Gas Turbine Institute (IGTI) of ASME for publication in the JOURNAL OF TURBOMACHINERY. Manuscript received July 7, 2014; final manuscript received July 21, 2014; published online August 26, 2014. Editor: Ronald Bunker.

TBC temperatures due to the insulating effect of the TBC. Davidson et al. [10] investigated the improvement in wall temperature when TBC was added to a matched Bi vane with Bi of 0.3–1.1. The cooling performance increased significantly with TBC to the point that increasing blowing ratio did not provide a further reduction in the vane wall temperature. A computational study of TBC applied to a conjugate wall with film cooling was completed by Na et al. [11]. The flat plate geometry contained a single 30 deg angled film cooling hole, and accounted for partial blockage of the film cooling hole by the TBC. Without TBC, the wall temperature was relatively uniform across the surface, indicating a low Bi, although the Bi was not stated. With TBC, decreased wall temperatures were reported.

Comparisons between experimental and computational conjugate heat transfer results are of increased interest since the experimental validation of the simulations provides an important designer tool. A study by Panda and Prasad [12] involved experimental measurements and computational simulations for a flat plate with internal impingement and film cooling. The simulations showed excellent agreement with the experimental results along the centerline. Plates with different thermal conductivities (plastic and stainless steel) were considered, but the Bi of these configurations were not reported. Dobrowolski et al. [13] performed conjugate simulations corresponding to the leading edge experiments without TBC by Maikell et al. [9]. The effect of impingement was applied by setting the internal wall temperature distribution to the temperatures measured in the experiments. Using the realizable $k-\epsilon$ turbulence model, the simulations underpredicted the separation of the film cooling jets compared to the experiments. Similar results were found for the same leading edge model with shaped film cooling holes and impingement [14,15].

The conjugate heat transfer through the suction side (SS) of a vane model (engine matched Bi of 0.4–1.6) was simulated by Ledezma et al. [16] using the standard $k-\omega$ turbulence model, and results were compared to experiments by Dees et al. [17]. Differences from the experiments were attributed to poor prediction of film cooling jet separation, the assumption of isotropic turbulence, and unsteady effects. The SS of a vane model with a similar Bi and impingement cooling was simulated by Dyson et al. [18] and compared to experiments in Williams et al. [19]. Film cooling jet diffusion was underpredicted by the SST $k-\omega$ turbulence model in the simulations. The insufficient diffusion led to overpredicted cooling effectiveness for attached jets and underpredicted effectiveness for detached jets. Ni et al. [20,21] simulated a fully film cooled vane and endwall geometry under flow conditions consistent with a dual spool engine with a pressure ratio of 40. The conjugate simulations were performed using the standard $k-\omega$ turbulence model. The predicted surface heat flux and temperature data agreed with the measurements within experimental uncertainties. The results showed significant temperature variations along the vane chord at 62% span.

Although there have been several studies comparing experimental and computational conjugate heat transfer results for different configurations, the current study fills two gaps in the literature. There are no studies comparing conjugate experiments and simulations for an endwall, and no studies which consider the effect of TBC on an endwall. The current study provides an experimental and computational comparison of a conjugate endwall with and without a TBC.

Conjugate Endwall Model

The endwall model in both the experimental and computational studies, as depicted in Fig. 1, incorporates the convective and solid conduction heat transfer associated with the following features: external film cooling, a TBC, a conducting endwall, and internal impingement jet cooling.

To obtain scaled temperature data that is engine relevant, the appropriate geometric, thermal, and flow parameters are taken into account. The relevant nondimensional parameters for a

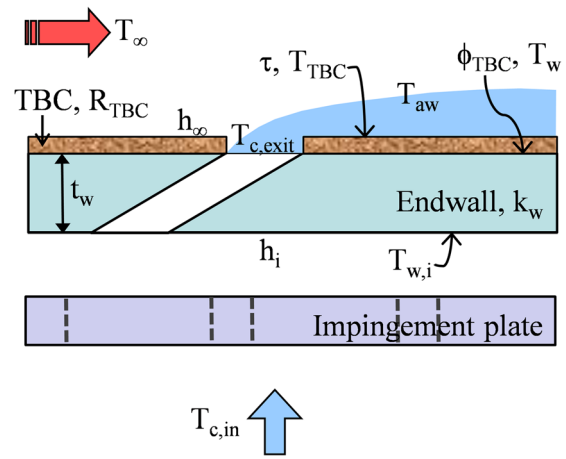


Fig. 1 Configuration of a conjugate endwall with impingement and film cooling and TBC

conducting wall with TBC are obtained from an expression derived for the nondimensional outer endwall temperature (at the interface between the endwall and the TBC) as the overall effectiveness with TBC, ϕ_{TBC} . The overall effectiveness is an important parameter to assess thermal performance because the airfoil life is dependent upon the outer wall temperature. The equation for ϕ_{TBC} , given in Eq. (1), is derived from a one-dimensional consideration of the heat transfer through the wall in Fig. 1. In the case of no TBC, the equation reduces to Eq. (2) for ϕ without TBC, previously reported in Refs. [2,19].

$$\phi_{TBC} = \frac{T_{\infty} - T_w}{T_{\infty} - T_{c,in}} = \frac{1 - \chi\eta}{1 + \frac{Bi + h_{\infty}/h_i}{Bi(R_{TBC}/R_w) + 1}} + \chi\eta \quad (1)$$

$$\phi = \frac{T_{\infty} - T_w}{T_{\infty} - T_{c,in}} = \frac{1 - \chi\eta}{1 + Bi + h_{\infty}/h_i} + \chi\eta \quad (2)$$

The dimensionless parameters revealed in Eqs. (1) and (2) include the endwall Bi, the h_{∞}/h_i , and the ratio of TBC to endwall thermal resistances (R_{TBC}/R_w), defined in the following equation:

$$R_{TBC}/R_w = \frac{R_{TBC}k_w}{t_w} \quad (3)$$

The overall effectiveness is also a function of the product of the coolant warming factor, χ , and the adiabatic effectiveness, η . Adiabatic effectiveness is commonly reported to indicate the effectiveness of external cooling techniques such as film cooling. Adiabatic effectiveness is assumed to be a function of geometry, the mainstream flow parameters, and film cooling flow parameters such as the film cooling blowing ratio, M . In Eqs. (1) and (2), η represents the nondimensional driving temperature for external convection in the presence of film cooling. The χ , defined in Eq. (4), is a correction factor for η that corrects for the warming of the coolant during impingement and flow through the film cooling holes, from $T_{c,in}$ to $T_{c,exit}$. As a result, the product, $\chi\eta$, and ϕ have the same normalizing temperature difference [19].

$$\chi = \frac{T_{\infty} - T_{c,exit}}{T_{\infty} - T_{c,in}} \quad (4)$$

Another quantity of interest when considering surfaces with TBC, is the scaled external temperature of the TBC, also known as the TBC effectiveness, τ , which is defined in the following equation:

Table 1 Conjugate endwall and TBC parameters

Parameter	Model	Typical engine
M_{avg}	0.6, 1.0, 2.0	1.0–2.0
k_w , W/m K	0.99–1.06	22
t_w , cm	1.27	0.20
$Bi = h_{\infty} t_w / k_w$	0.3–0.7 [22]	0.27
h_{∞} / h_i	$M = 0.6$ 1.1–2.3 [22,23] $M = 1.0$ 0.7–1.4 [22,23] $M = 2.0$ 0.5–1.1 [22,23]	1.0
R_{TBC} , m ² K/W	0.035 [24]	8×10^{-5} – 9×10^{-4} [1,25–27]
R_{TBC} / R_w	2.5	0.6–9.3

$$\tau = \frac{T_{\infty} - T_{TBC}}{T_{\infty} - T_{c,in}} \quad (5)$$

Since T_{TBC} is on the same heat transfer circuit used to derive Eq. (1), it follows that τ depends on the same parameters as ϕ_{TBC} .

The nondimensional parameters matched to an engine for the endwall and TBC layer for both the experiments and simulations in this study are given in Table 1. The blowing ratio, M_{avg} , which affects $\gamma\eta$, defines the average ratio of coolant to mainstream mass flux. The endwall h_{∞} distribution is obtained from measurements made by Lynch et al. [22]. An engine matched Bi is achieved by making the endwall from Corian®, a DuPont material. To estimate h_i for each blowing ratio, a Nu correlation, derived by Hollworth and Dagan [23] for an impingement array with staggered coolant extraction, is used. The thermal effect of a TBC is reproduced with a thin layer of cork. The conductivity and thickness of the cork have been chosen to replicate the R_{TBC} / R_w within the range of a typical engine.

Experimental Methods

Overall effectiveness (ϕ) and TBC effectiveness (τ) were measured for the endwall of a linear cascade in the corner test section of the large-scale, low-speed, closed loop wind tunnel shown in Fig. 2(a). This facility split the flow upstream of the cascade into mainstream and coolant streams. The mainstream section was heated by a heater bank and passed through flow conditioning elements including a turbulence grid $\sim 11C_{ax}$ upstream of the test section. A more detailed description of the wind tunnel and flow conditioning elements can be found in Ref. [22]. The mainstream temperature was measured $0.52C_{ax}$ in the axial direction upstream of the blades at multiple spanwise and pitchwise locations with a thermocouple rake. The mainstream temperature varied by no more than $\pm 0.6^{\circ}C$ from the average T_{∞} . A Pitot probe, also inserted $0.5C_{ax}$ upstream, was used to measure the inlet mainstream velocity, U_{∞} . The standard deviation over the mean U_{∞} was less than 1%.

The coolant passed through a desiccant drier and two heat exchangers that chilled the coolant, before entering the plenum located below the endwall. A laminar flow element, directly measured the total coolant flowrate, which was adjusted to achieve the necessary blowing ratios. The blowing ratios reported in this study, M_{avg} , were an average of the local M at each film cooling hole. The uncertainty in coolant flowrate was estimated for a 95% confidence interval as $\pm 3\%$, using sequential perturbation [28]. To measure the internal coolant temperature, $T_{c,in}$, there were two thermocouples located approximately $8.7D$ below the impingement plate, which agreed within $\pm 3^{\circ}C$. The experimental setup achieved a typical mainstream to coolant temperature difference of $40^{\circ}C$, which provided a coolant to mainstream density ratio of about 1.15.

The test section contained a seven blade linear cascade based on the low-pressure turbine Pack-B airfoil, which has been used in many other studies [2,8,22,29–37]. Figure 2(b) shows the top

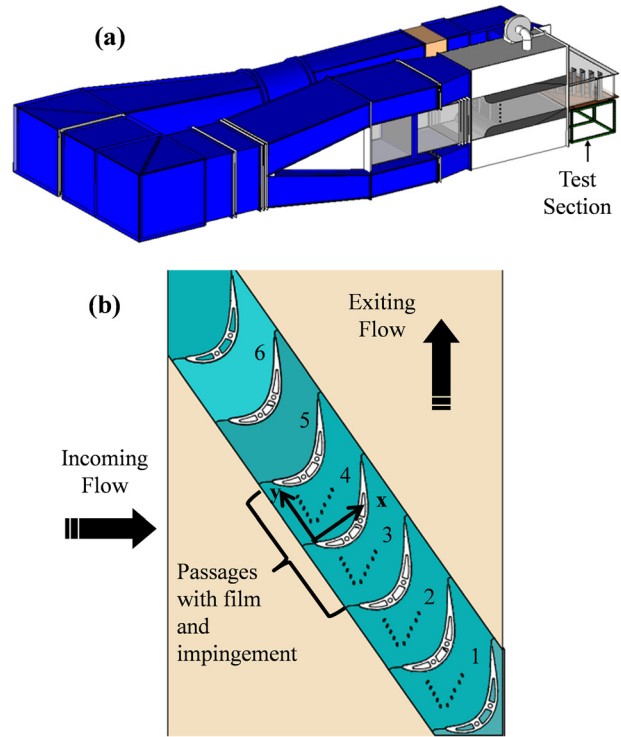


Fig. 2 Depiction of (a) the large-scale low-speed wind tunnel and (b) the test section containing the Pack-B linear blade cascade and conjugate endwall

view of the test section including the shaded part of the endwall constructed from Corian. Outside of the passage, the endwall was constructed from medium density fiberboard (MDF). The center passages, 3 and 4, had film and impingement cooling and were used for this study. A summary of the blade geometry and mainstream flow conditions is given in Table 2. At $0.5C_{ax}$ upstream of the blade leading edge in the axial direction, the δ_{99}/S was 0.089 and the freestream turbulence was 7%, as predicted by the CFD solution from this study. The details of the simulations are described in the Computational Methodology section.

Periodicity of the cascade was determined by taking measurements of the pressure distribution at the midspan of all seven blades. In Fig. 3, a typical set of data for the pressure coefficient, C_p , is plotted versus normalized axial distance. The measured C_p agreed well with the CFD results from this study, as well as with an inviscid 2D CFD prediction from Ref. [22].

The endwall configuration was designed with a generic internal and external cooling geometry to replicate the relevant nondimensional parameters given in Table 1. Figure 4(a) shows the side view of the plenum, cooling features, endwall, and the layer of TBC. A splash plate was used in the experiments to spread and slow the plenum inlet flow. The coolant passed through an impingement plate with 28 staggered holes. The nondimensional height between the impingement plate and the bottom of the endwall, was $H/D = 2.9$. Following impingement, the coolant flowed into ten angled film cooling holes, which were staggered between the impingement holes. The diameter, D , of the impingement and

Table 2 Flow conditions and blade geometry

Scale factor	8.6	Inlet U_{∞}	10.5 m/s
C_{ax}	0.218 m	Inlet, flow angle	35 deg
p/C_{ax}	0.826	Exit flow angle	60 deg
S/C_{ax}	2.50	Inlet Ma	0.029
Inlet Re	1.22×10^5	Exit Ma	0.047
Exit Re	1.98×10^5		

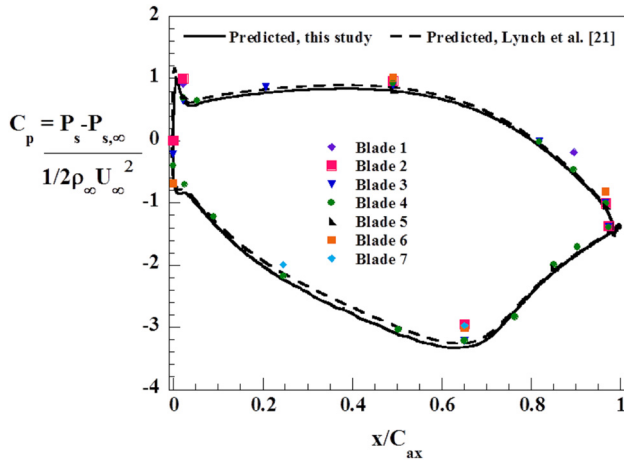


Fig. 3 Pack-B cascade static pressure distribution at the blade midspan compared to CFD predictions

film cooling holes was 4.4 mm. The film cooling holes were angled at 30 deg to the surface, resulting in a hole length to diameter ratio, L/D , of 5.8. The locations of the film holes and impingement jets are given in Fig. 4(b). The spacing of the impingement holes in the pitch (y) direction was 4.65D, and the spacing of the impingement rows in the axial (x) direction was 4.65D. The film cooling holes were oriented in the x - y plane to align with endwall streaklines reported in Ref. [22].

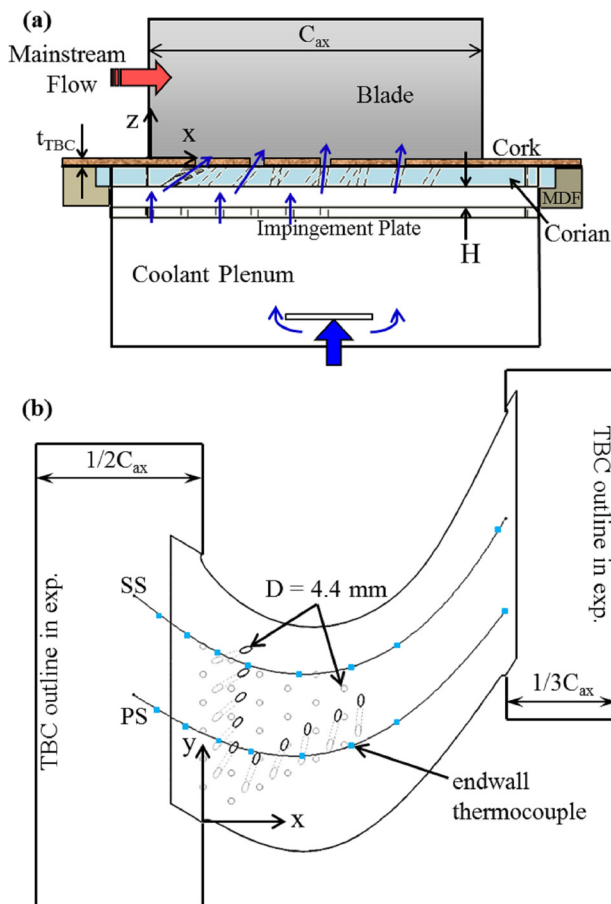


Fig. 4 Schematic of internal and external cooling scheme from (a) the side view and (b) the top view showing the outline of the TBC and discrete thermocouple measurements taken on the endwall in the experiments

In experiments with TBC, the cork layer extends $1/2C_{ax}$ upstream of the blade leading edge and $1/3C_{ax}$ downstream of the trailing edge as illustrated in Fig. 4(b). The thickness of the cork, t_{TBC} , is $0.45D$. The cork is adhered to the endwall using several layers of contact cement to replicate the adhesive methods for which the thermal resistance for the combined cork and adhesive layer was given in Table 1.

The steady-state external surface temperature was measured using infrared (IR) thermography with a FLIR P20 IR camera. This technique was capable of achieving a high spatial resolution of 5.7 pixels/D. Additional details regarding the IR measurement technique and calibration are available in Mensch and Thole [2]. The external surface temperatures were scaled to ϕ for the cases without TBC, and scaled to τ for the cases with TBC. The uncertainty in the external effectiveness was estimated to be ± 0.02 for a 95% confidence interval [2].

To determine the outer endwall temperature for ϕ_{TBC} , 16 thermocouples were installed to measure the temperature at the interface between the endwall and the cork layer. A high conductivity epoxy, $k = 4.3$ W/m K, was used to attach the thermocouples to the endwall at the locations shown as blue squares in Fig. 4(b). These points followed two inviscid streamlines referred to hereafter as suction side (SS) and pressure side (PS) streamlines. Using a 95% confidence interval, the uncertainty in ϕ_{TBC} was estimated to be ± 0.01 , since temperature measurements were made directly with thermocouples.

Computational Methodology

Conjugate simulations for the endwall with and without TBC were performed using the commercial CFD software FLUENT [38]. The segregated pressure-based SIMPLE algorithm was used to solve the steady-state Reynolds-averaged Navier–Stokes (RANS) and energy equations using the SST $k-\omega$ turbulence model [39] for closure with second-order spatial discretization schemes. The SST $k-\omega$ model was chosen because it has shown reasonable agreement with experimental results in turbomachinery applications [8,12,18,40,41].

The computational grid began $3.5C_{ax}$ upstream of the blade leading edge in the inlet flow direction to capture the flow development upstream of the cascade, as shown in Fig. 5(a). At this location, a velocity inlet was applied with a freestream velocity of 10.5 m/s and a boundary layer profile benchmarked to the measurements by Lynch et al. [22]. The inlet velocity, turbulent kinetic energy, and specific dissipation profiles were generated using the boundary layer code TEXSTAN [42] to match the measured momentum thickness Reynolds number, $Re_{\theta} = 1330$, at the measurement location $2.85C_{ax}$ upstream of the blade leading edge [22]. The temperature at the inlet reflected the typical T_{∞} in the experiments. An outflow boundary condition was applied $1.5C_{ax}$ downstream of the blade trailing edge in the axial direction. Symmetry was imposed at the top of the domain, which is located at the midspan of the blade in the experiments. A single blade passage was simulated using periodic boundaries that extended vertically through the entire domain, cutting through the mainstream section, the TBC and endwall, four film cooling holes, the impingement channel, and the plenum.

A mass flow inlet boundary condition was applied at the bottom of the computational plenum, which was located $65D$ below the impingement plate to reflect the dimensions of the plenum in the experiments. The mass flow rate and temperature applied at the boundary matched the conditions in the experiment for that blowing ratio. Blowing ratios of 1 and 2 were simulated. Air properties used for the flow were incompressible-ideal gas for density, polynomial fits to temperature for thermal conductivity and specific heat, and Sutherland's law for viscosity. The properties used for the solids are listed in Table 1.

A thermally coupled wall interface was used at all conjugate solid/fluid boundaries. For the simulation with TBC, a cork layer extended along the entire endwall surface of the computational domain except for the film cooling holes. A thermally coupled

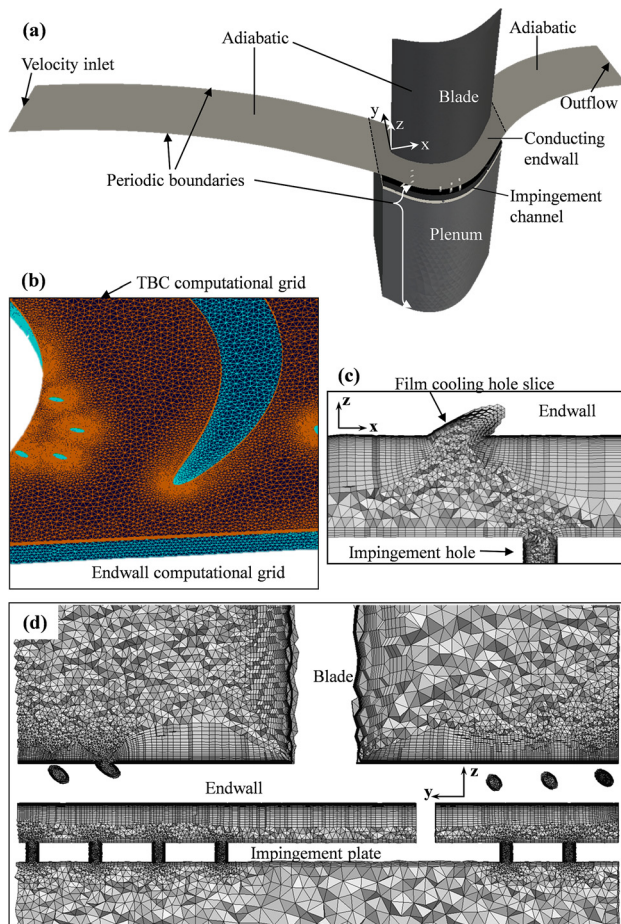


Fig. 5 Depiction of (a) the computational domain and boundary conditions, (b) the surface grid for the endwall and TBC, (c) the prism layer volume grid in the holes and impingement channel, and (d) the volume grid in the mainstream, channel, and plenum

wall interface was also used at the boundary between the TBC and the endwall. All other wall surfaces in the domain were modeled as adiabatic.

Separate unstructured grids were generated for the conducting endwall solid, the conducting TBC solid, and the flow domain. The commercial grid generation software, Pointwise [43], was used to generate the unstructured grids for the endwall and TBC geometries, shown in Fig. 5(b). The endwall grid contained 1.5×10^6 cells, and the cork grid contained 0.3×10^6 cells. For the flow domain, the Advancing-Front/Local-Reconnection unstructured grid generation software, AFLR3 [44], was used to create a high-fidelity tetrahedral grid with wall-normal prism layers to resolve the boundary layer on key surfaces (the blade, the entire external endwall surface, the internal endwall surface, the film cooling holes, and the impingement holes) with a wall spacing such that $y^+ < 1$. The unstructured grid for the flow is depicted in Fig. 5(c), showing a slice in the y -plane through a film cooling hole inlet and an impingement hole, and in Fig. 5(d), showing a slice in the x -plane through the mainstream, film cooling holes, impingement channel, impingement holes, and plenum. The initial grid size for the flow domain was 9.8×10^6 cells.

Convergence of a simulation was achieved when the normalized residuals were $> 1 \times 10^{-4}$ and the area-averaged endwall ϕ changed by less than 0.0015 over 500 iterations. To ensure grid independence, the initial grid without TBC that contained a total of 11.3×10^6 cells was uniformly refined to a grid containing a

total of 18.5×10^6 cells. The difference in the solution for the area-averaged ϕ over the endwall from the refined grid relative to the initial grid was 1×10^{-4} for $M_{\text{avg}} = 1.0$. Also, the total heat flux at the internal endwall surface varied by less than 0.25% for the refined grid relative to the initial, nominal grid. Thus, it was concluded that the nominal grid was of sufficient resolution for the present conjugate heat transfer predictions, and the CFD solutions were grid insensitive.

Results and Discussion

The effects of blowing ratio, M , and the TBC are examined through measurements and steady-state RANS predictions of overall effectiveness without TBC (ϕ) and with TBC (ϕ_{TBC}), in addition to the TBC effectiveness, τ . The predictions reveal heat flux and temperature trends that can be used to understand the physical mechanisms involved in the conjugate endwall heat transfer.

Measured and Predicted Temperatures Without TBC. The contours of overall effectiveness, ϕ (nondimensional endwall temperatures) for two blowing ratios of $M_{\text{avg}} = 1.0$ and 2.0 are shown in Figs. 6 and 7. The contours show the nondimensional endwall temperatures measured without TBC (Figs. 6(a) and 7(a)) and predicted without TBC (Figs. 6(b) and 7(b)). Also, Figs. 6(c) and 7(c) show the predicted endwall temperatures under the TBC, ϕ_{TBC} , which will be discussed in the following section, Measured and Predicted Temperatures With TBC. The film cooling holes and plenum boundaries are shown for reference in Figs. 6 and 7. The horizontal lines just below each blade indicate a wall in the impingement channel that prevents coolant from crossing into another passage after passing through the impingement plate. Note that the experimental results are shown for two passages, indicating good periodicity. For comparison to the measurements, repeated images are shown for the predictions.

For $M_{\text{avg}} = 1.0$ the area-averaged \bar{Nu} across entire internal end-wall surface is predicted to be 3.2 without TBC. With TBC, the difference is only 0.1%, showing that the CFD is consistent with the internal flow predictions. Likewise the predicted internal \bar{Nu} for $M_{\text{avg}} = 2.0$ is nearly the same with and without TBC, with a value of 5.2 for both cases and a difference of 0.4%. It is expected that the external heat transfer coefficients do not change between the cases with and without TBC since the flowfield did not change.

The comparison of the measured and predicted endwall temperature (ϕ) contours without TBC (Figs. 6(a) and 6(b) and Figs. 7(a) and 7(b)) at both blowing ratios are very good. The simulations correctly predict the extent of lateral conduction into the uncooled areas. As seen in Figs. 6(a) and 6(b) at $M_{\text{avg}} = 1.0$, there are some discrepancies between the measured and predicted ϕ in the areas with film cooling. As many other studies have found, RANS CFD often has difficulty predicting mixing in the film cooling jet shear layer and predicting film attachment. For $M_{\text{avg}} = 2.0$ in Figs. 7(a) and 7(b), a small difference can be seen in the influence of the film cooling jets closest to the SS. Although the CFD correctly predicts the jet detachment, the predicted ϕ here is less than the measured ϕ . The simulations are underpredicting the cooling influence that the detached jets have on the wall, a trend also observed by Dyson et al. [18]. However, the strong effect of in-hole convection at $M_{\text{avg}} = 2.0$ is well predicted in the high ϕ at the exits of the film cooling holes.

A small difference in ϕ is also seen downstream in the passage for both blowing ratios. In the downstream region of Figs. 6(b) and 7(b), the simulations show a slightly lower ϕ (by about 0.05) and a warmer endwall than the experiment. These differences are attributed to small heat losses present in the experiment that are not captured in the simulation. An example of a surface modeled as adiabatic that loses heat to the surrounding environment is the downstream side of the Corian endwall. The endwall is surrounded on the side and bottom by MDF shown in Fig. 4(a).

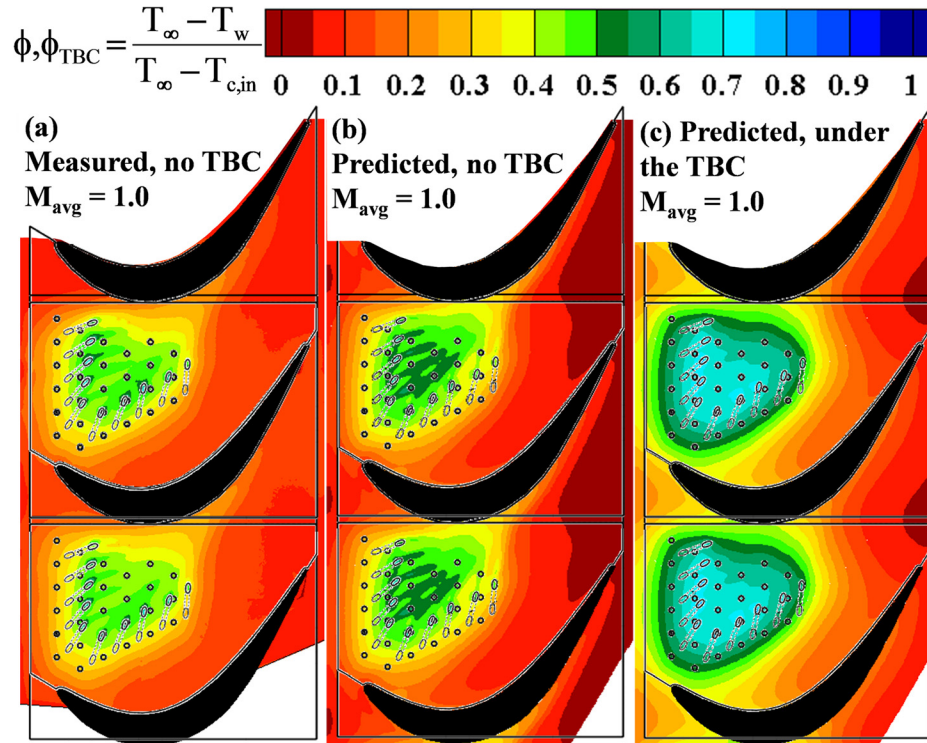


Fig. 6 Overall effectiveness contours for $M_{avg} = 1.0$ (a) measured without TBC, (b) predicted without TBC, and (c) predicted under the TBC

The conduction heat loss from the downstream sides of the endwall into the fiberboard ($k = 0.3 \text{ W/m}^2$) is estimated to be on the same order as the convective heat transfer into the endwall from the mainstream. The lateral conduction in this part of the endwall is estimated to be an order of magnitude less because the temperature gradients in this region of the endwall are small. By using

adiabatic boundary conditions in the simulations, the steady-state endwall temperature is higher than measured in the experiments.

The data in Figs. 8(a)–8(f) give the local ϕ along the length of the PS and SS streamlines shown in Fig. 4(b). The experimental ϕ without TBC and the predicted ϕ (in red) have been extracted from the measured and predicted contours in Figs. 6 and 7. The measured

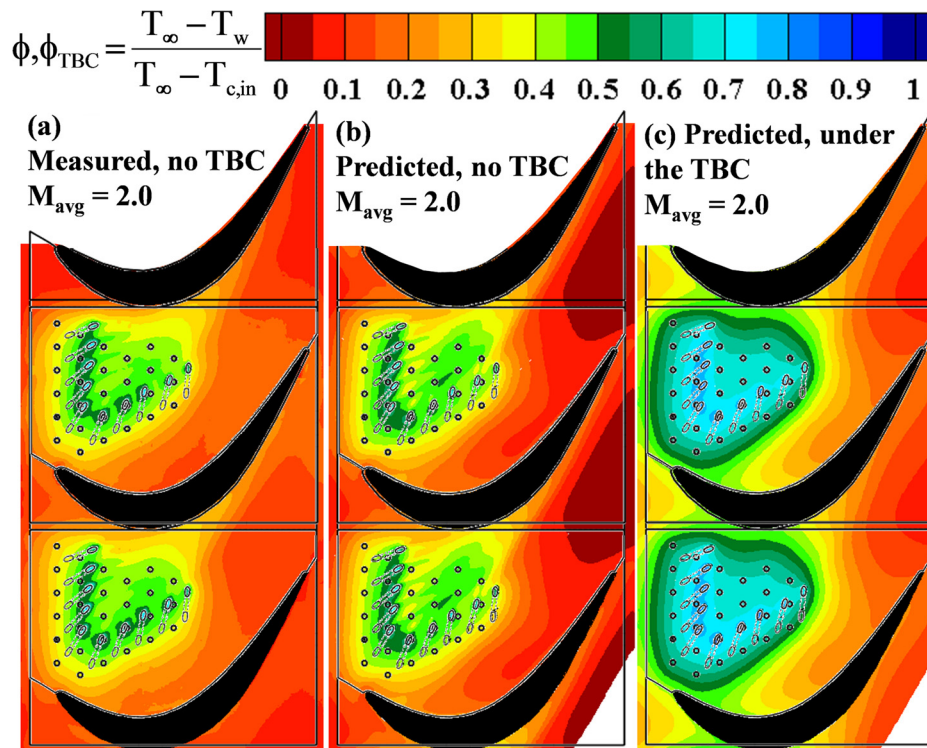


Fig. 7 Overall effectiveness contours for $M_{avg} = 2.0$ (a) measured without TBC, (b) predicted without TBC, and (c) predicted under the TBC

and predicted ϕ_{TBC} will be discussed in the next section, Measured and Predicted Temperatures With TBC. For $M_{avg} = 0.6$, the experimental data are shown in Fig. 8(a) for the PS and Fig. 8(d) for the SS. (No CFD simulations were done at the lowest blowing ratio.) Similar graphs are shown for $M_{avg} = 1.0$ in Figs. 8(b) and 8(e) and for $M_{avg} = 2.0$ in Figs. 8(c) and 8(f). A repeated data set is shown for $M_{avg} = 1.0$ in Figs. 8(b) and 8(e) for the experiments with and without TBC. The excellent agreement between repeated experiments indicates the experiments are reproducible.

As expected from the contours, the predicted ϕ shows good agreement with the measurements, especially on the PS (Figs. 8(b) and 8(c)). The PS streamline crosses a few film cooling holes at or just upstream of the hole exits, which show up as sharp peaks in the graphs. Other than at these peaks, the endwall along the PS streamline is influenced by internal cooling only. Both effects of internal impingement and in-hole convection increase with blowing ratio, which is well captured by the predictions.

The agreement on the SS is not as close as on the PS because the SS streamline crosses the downstream path of several film cooling jets. The SS ϕ data, shown in Figs. 8(d)–8(f), have a sharp drop around $s/C_{ax} = 0.2$ following a film cooling hole. At $M_{avg} = 0.6$ (Fig. 8(d)), the SS line continues to slowly decrease consistent with the behavior of an attached film cooling jet. As blowing ratio increases (Figs. 8(e) and 8(f)), the ϕ behavior reflects that of a detached and reattached jet because ϕ slightly increases again following the sharp drop. For $M_{avg} = 1.0$ between s/C_{ax} of 0.1–0.5 (Fig. 8(e)), the simulations overpredict the increase in ϕ associated with reattachment of the film cooling jets. For $M_{avg} = 2.0$, there is a slight underprediction of ϕ on the SS (Fig. 8(f)) around s/C_{ax} of 0.1–0.3, which is related to the deficiency of RANS in correctly predicting the diffusion of detached film cooling jets to provide some cooling to the wall.

The data obtained in the simulations can be used to provide more insight into the conjugate heat transfer in locations where it is difficult to obtain experimental measurements. The predicted distributions of dimensionless temperature within the endwall and the impingement channel are revealed in Fig. 9 through two slices of the domain. Figure 9(a) shows the slices at the leading edge of the blade, $x/C_{ax} = 0$, which also line up with the first row of impingement holes. The slices shown in Fig. 9(b) are located at $x/C_{ax} = 0.09$, which passes through the second row of impingement holes and also partway through five film cooling holes. Both sets of slices display the impingement plate and the separating wall in the impingement channel in white, since these features are nonconducting.

From Fig. 9, it is observed that impingement and in-hole convection become more effective with the increase in blowing ratio. Figure 9(a) shows that the first row of impingement holes is very effective at cooling the endwall. Just above the bottom of the endwall, the temperature contours show the effect of individual impingement jets, but at the top of the endwall, the cooling has spread and the wall temperature is more uniform than at the bottom. In Fig. 9(b), the effect of the in-hole convective cooling on the wall is shown. The temperature contours bend as they encounter a film cooling hole because there is significant heat transfer at the hole surface. The temperature contours also give an indication of the flow patterns of the impingement jets in the channel. The coolant impinges on the internal side of the endwall, and then flows outward, and down towards the impingement plate as it encounters the flow from the adjacent jets. The flow moving towards the impingement plate has picked up heat from the endwall and is warmed slightly.

Measured and Predicted Temperatures With TBC. The layer of TBC prevents optical access to the endwall surface so the

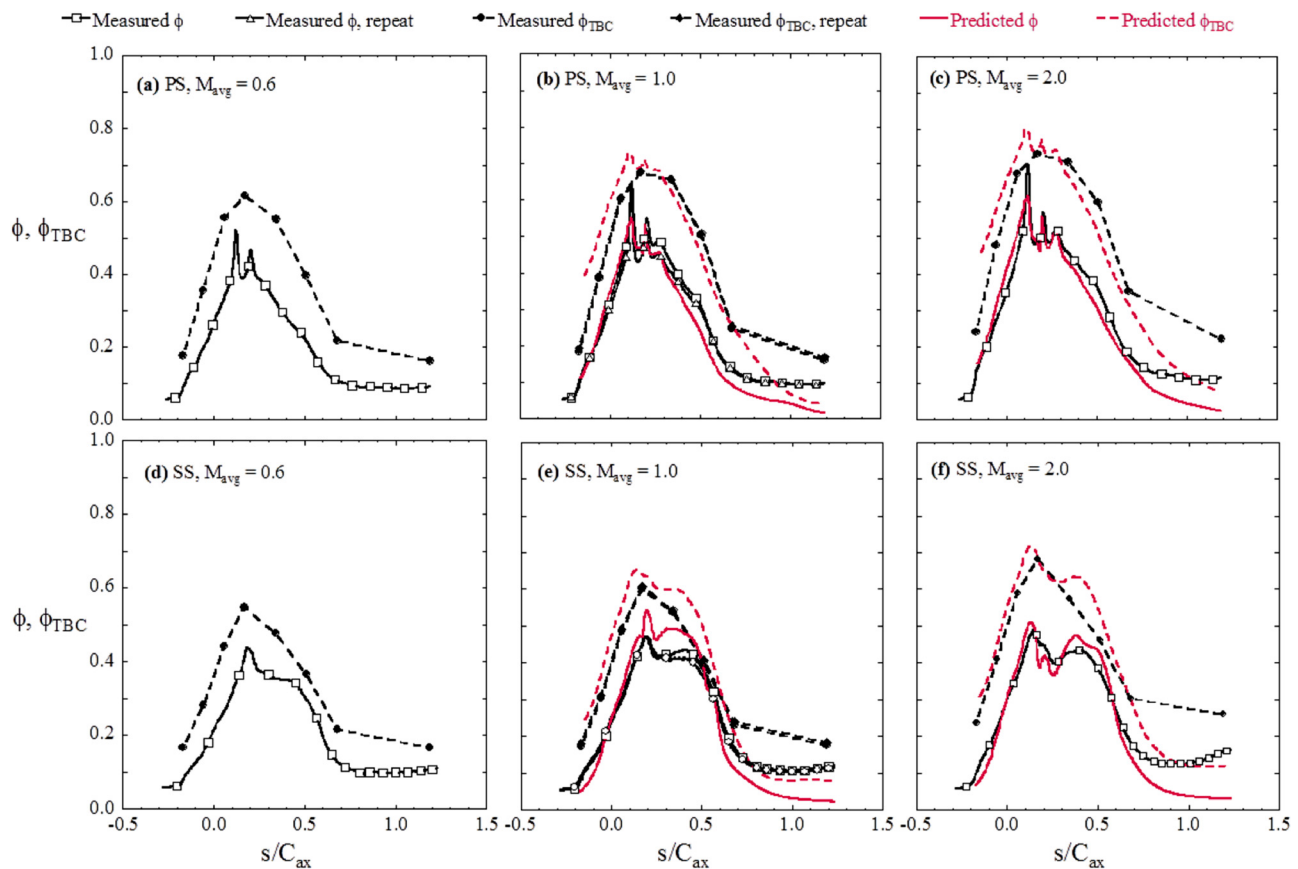


Fig. 8 Comparison of overall effectiveness with and without TBC, showing measured and predicted values, along inviscid streamlines, PS (a)–(c) and SS (d)–(f)

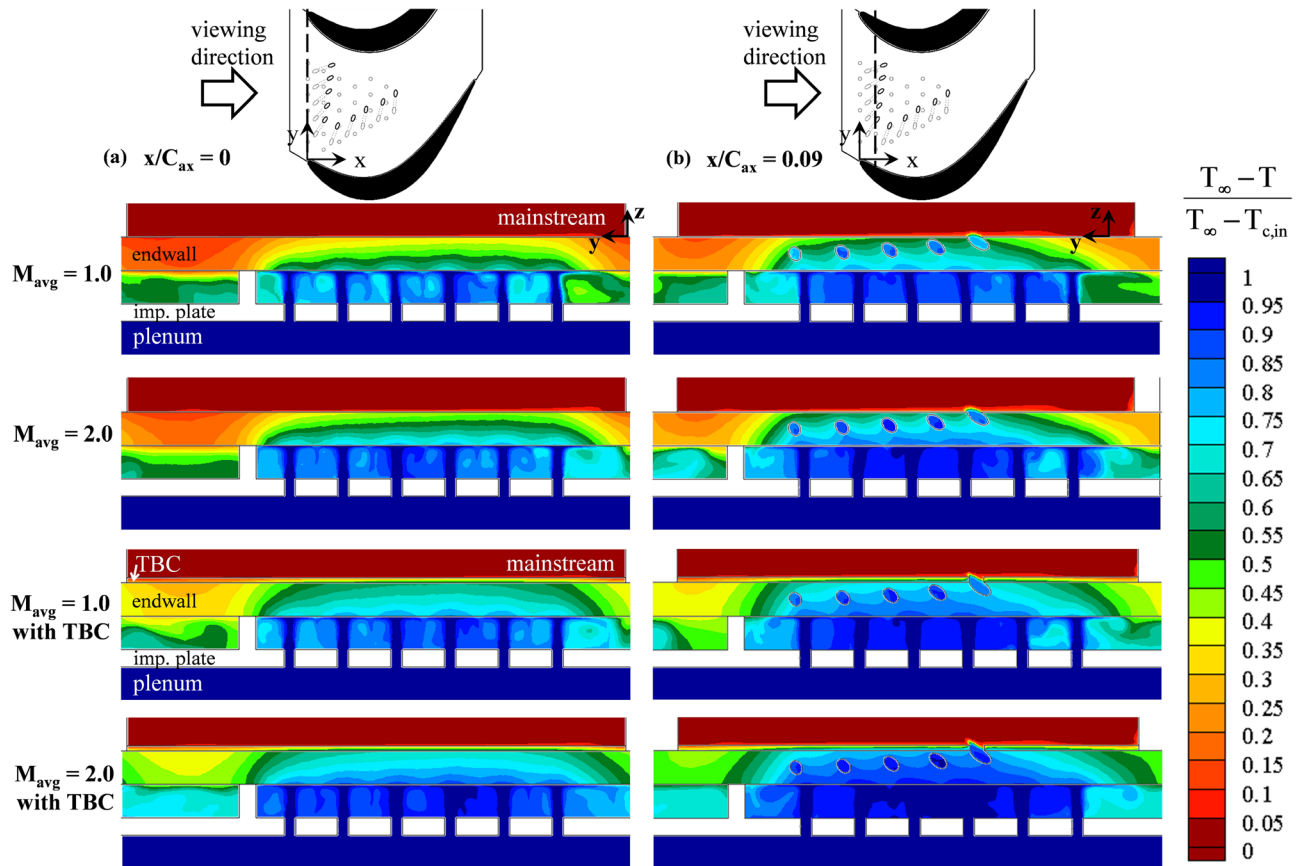


Fig. 9 Conjugate CFD prediction of nondimensional temperature in the fluid and the solid at different two slices (a) at the first row of impingement holes and (b) at the second row of impingement holes

IR camera cannot measure ϕ_{TBC} on the endwall. Therefore, the measured ϕ_{TBC} is compared to the case without TBC in Figs. 8(a)–8(f) for the discrete thermocouple measurements made below the TBC along the inviscid streamlines. Along the inviscid streamlines, higher cooling performance is observed with TBC compared to no TBC for all three blowing ratios. TBC increases the effectiveness on the PS line at all measurement locations by nearly a constant amount. The increase from ϕ to ϕ_{TBC} varies on the SS along the length of the streamline, especially between $0.2 < s/C_{ax} < 0.7$. The local peaks from film cooling seen on the endwall without TBC have been smeared out in ϕ_{TBC} because the TBC is insulating the endwall from the external flow, which includes film cooling.

The predictions of ϕ_{TBC} in Figs. 6(c), 7(c), 8(b), 8(c), 8(e), 8(f), 9(a), and 9(b) also show that the TBC provides a significant cooling effect on the endwall. The predicted contours of ϕ_{TBC} for $M_{avg} = 1.0$, in Fig. 6(c) and for $M_{avg} = 2.0$ in Fig. 7(c), are significantly higher at all locations on the endwall relative to ϕ without TBC. When the blowing ratio is increased from $M_{avg} = 1.0$ (Fig. 6(c)) to $M_{avg} = 2.0$ (Fig. 7(c)), the area of high effectiveness under the TBC increases. The predicted ϕ_{TBC} along the inviscid streamlines in Figs. 8(b), 8(c), 8(e), and 8(f) (dashed red lines) compare fairly well with the discrete ϕ_{TBC} measurements. The predictions show some influence of the film cooling on ϕ_{TBC} , which is not observed in the measurements. Both ϕ_{TBC} and ϕ are underpredicted downstream in the passage for $s/C_{ax} > 0.7$. These discrepancies are attributed to the conduction losses at the endwall sides previously discussed in reference to the ϕ contours. When TBC is included in the slices of nondimensional temperature in Fig. 9, the endwall temperatures are greatly reduced, even in the areas not around the impingement and film cooling holes. In addition, the fluid in the channel and the film cooling holes remains cooler with TBC than the cases without TBC. When TBC is

added, there is less warming of the coolant because the TBC reduces the internal wall temperature.

The average increases in ϕ due to changes in the blowing ratio and due to the addition of TBC are compared in Table 3. The change due to M , $\Delta\phi_M$, is an area-average across the impingement area from Mensch and Thole [2]. The change due to TBC, $\Delta\phi_{TBC}$, is the average difference between ϕ_{TBC} and ϕ (without TBC) at the measurement locations along the streamlines. The values in the table show that the improvement due to the addition of TBC is about three times greater than the improvement from increasing blowing ratio. Changing blowing ratio is less effective than TBC at reducing endwall temperatures, which is consistent with the findings on the vane surface [10].

The improvement in ϕ due to the TBC for the measurements and simulations has been plotted in Fig. 10. The values for the experiment are those given in Table 3. The predicted data are an average across the entire conducting endwall surface. Figure 10 demonstrates that $\Delta\phi_{TBC}$ slightly increases with blowing ratio. The measured and predicted values for improvement with TBC agree very well, indicating that the discrete thermocouple locations used to measure the endwall temperatures under the TBC provide a good indication of the effect throughout the passage.

Table 3 Measured improvement in overall effectiveness due to increase in M or due to addition of TBC

ΔM	$\Delta\phi_M$ [2]	M_{avg}	$\Delta\phi_{TBC} = \phi_{TBC} - \phi$
0.6–1.0	0.05	0.6	0.13
		1.0	0.14
1.0–2.0	0.04	2.0	0.17

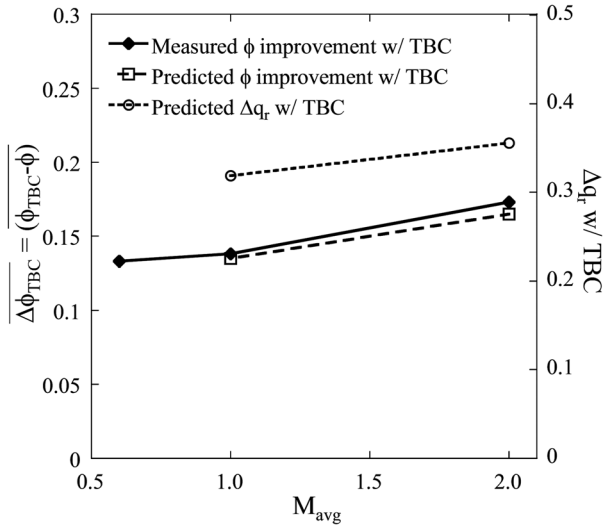


Fig. 10 Measured and predicted improvement with TBC, $\Delta\phi_{TBC}$, and the predicted Δq_r for the external endwall surface plotted as a function of M_{avg}

The net heat flux reduction with TBC, Δq_r , can be calculated at the endwall outer surface using the following equation:

$$\Delta q_r = \frac{q_w - q_{w,TBC}}{q_w} \quad (6)$$

The predicted Δq_r is plotted on Fig. 10 for the y-axis on the right side of the figure. The simulations predict that Δq_r also increases with blowing ratio. Similar trends are found for Δq_r when applied to the other endwall surfaces (the internal endwall surface and the surfaces of the film cooling holes). Therefore, adding TBC gives a greater reduction in q_w , and a greater improvement in ϕ at higher blowing ratios. With TBC, the endwall is insulated from the hot mainstream, but still influenced by the internal cooling. As blowing ratio increases, the internal impingement and in-hole convection cooling become more effective, generating higher heat transfer coefficients, and bringing the endwall temperatures closer to the coolant temperature, as can be seen in the temperature slices in Fig. 9. Therefore, the insulating effect of the TBC provides a greater benefit for cases that have higher heat transfer without TBC, which are the cases with higher M and h_i .

The measured and predicted dimensionless temperatures on the outer TBC surface, τ , are shown in Fig. 11. Experimental measurements are shown for three blowing ratios, including Fig. 11(a) at $M_{avg}=0.6$, Fig. 11(b) at $M_{avg}=1.0$, and Fig. 11(c) at $M_{avg}=2.0$. Similarly, computational predictions are given in Fig. 11(d) for $M_{avg}=1.0$ and Fig. 11(e) for $M_{avg}=2.0$. Because the TBC has a higher thermal resistance than the endwall, τ is generally lower than ϕ and is closer in appearance to the effectiveness for an adiabatic wall, η . However, as blowing ratio increases, impingement and in-hole convection begin to have a greater effect on τ . The insulating effect of TBC is also observed in the lower temperatures measured at the exit of the holes compared to the cases without TBC (shown in Figs. 6 and 7). The reduction in coolant warming with TBC is also observed in the temperature slices in Fig. 9.

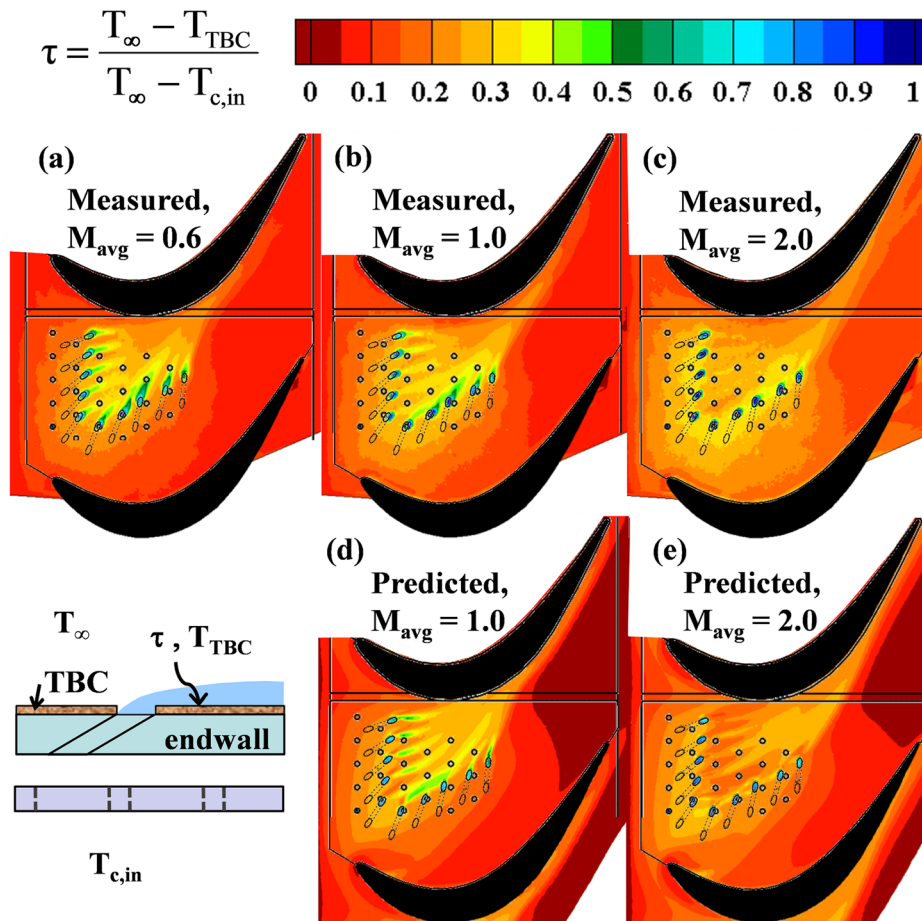


Fig. 11 Contours of TBC effectiveness at three blowing ratios, (a) measured $M_{avg}=0.6$, (b) measured $M_{avg}=1.0$, (c) measured $M_{avg}=2.0$, (d) predicted $M_{avg}=1.0$, and (e) predicted $M_{avg}=2.0$

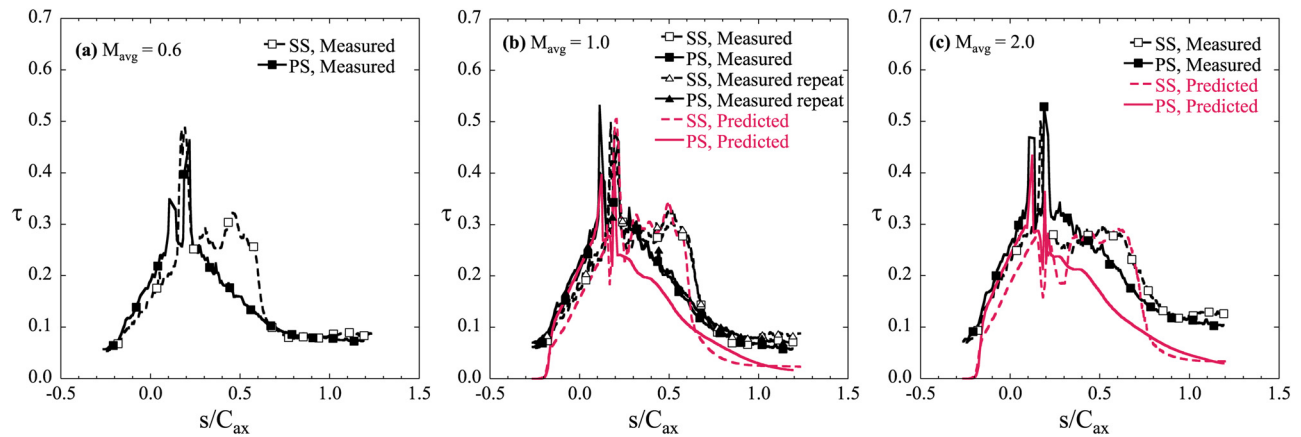


Fig. 12 Comparison of TBC effectiveness with film and impingement cooling, showing measured and predicted values, along inviscid streamlines, for (a) $M_{avg} = 0.6$, (b) $M_{avg} = 1.0$, and (c) $M_{avg} = 2.0$

The corresponding predictions for τ show reasonable agreement to the experiments. Like the measurements, the simulations predict temperatures on the outside of the TBC to be hotter than the bare endwall. However, the predicted τ is slightly lower than measured, especially for $M_{avg} = 2.0$. Also, the simulation for $M_{avg} = 1.0$ in Fig. 11(d) shows more jet attachment than the experiments, which is consistent with the ϕ comparison at the same blowing ratio. The fully detached jets for $M_{avg} = 2.0$ in Fig. 11(e) have less influence on τ compared to the experiments, a trend that was also observed for ϕ .

The external TBC temperatures, τ , along the inviscid SS and PS streamlines are given in Fig. 12(a) for $M_{avg} = 0.6$, Fig. 12(b) for $M_{avg} = 1.0$, and Fig. 12(c) for $M_{avg} = 2.0$. The data within the film cooling hole outlets have been removed. As blowing ratio increases, the SS data (dashed lines) do not increase because the film cooling jets become detached from the TBC surface. The decreased cooling by the film jets is balanced by the increased cooling by internal impingement. In contrast, the PS data increase with each increase in blowing ratio because the PS streamline does not cross the path of the film cooling jets, and is influenced by internal cooling. As discussed in reference to the contours, the simulations predict lower τ than measured and less influence on τ by the internal cooling than the experiments indicate. This is more apparent on the PS after $s/C_{ax} > 0.25$, and on the SS after $s/C_{ax} > 0.7$, downstream of the film cooling jets. Despite the underprediction, the trends of the data in the passage are well captured by the simulations.

Conclusions

Overall and TBC effectiveness measurements were compared to conjugate CFD predictions for the cases with and without TBC at different blowing ratios. The improvement in overall effectiveness due to TBC was evaluated and found to be significant. Adding TBC produced a greater improvement in overall effectiveness than the improvements achieved by increasing blowing ratio alone. The TBC protected the endwall from the hot mainstream, reduced heat transfer, and allowed the internal cooling to be more effective. As blowing ratio increased, a greater improvement in overall effectiveness was observed because the TBC was more effective at reducing heat transfer when the heat transfer was higher without TBC. The reduction in heat transfer with TBC also caused the outer TBC temperature to be higher in comparison to the endwall temperature without TBC.

The predicted overall effectiveness with no TBC showed good agreement with the measurements. The main differences were observed in the prediction of film cooling jet attachment for $M_{avg} = 1.0$ and diffusion for $M_{avg} = 2.0$, which were consistent with previous literature findings. The predictions of TBC

effectiveness were reasonably close to the measurements, and the correct trends were captured by the simulations. In conclusion, the predictive model in conjunction with a suitable grid gave reasonable predictions of conjugate heat transfer on an endwall.

The simulations were used to reveal the temperature behavior within the impingement channel and the endwall. The temperature contours showed that the heat transfer was highly three-dimensional, and steep temperature gradients existed in the wall. The effects of individual impingement jets and film cooling holes were observed inside the wall through the thermal gradients. The predicted temperature distributions inside the wall and impingement channel demonstrated the importance of matching the relevant nondimensional parameters in a conjugate model.

Acknowledgment

The authors would like to acknowledge support from the U.S. Department of Energy (DOE), National Energy Technology Laboratory (NETL) through the University Turbine Systems Research (UTSR) program. Any opinions, findings, conclusions, or recommendations expressed herein are solely those of the authors and do not necessarily reflect the views of the DOE. The writers would like to thank Mark Zelesky of Pratt & Whitney, Dr. David Bogard of the University of Texas, and Robin Ames of DOE-NETL for their continued communication and support regarding this research.

Nomenclature

- Bi = Biot number ($h_{\infty}t/k_w$)
- C_{ax} = axial chord length
- C_p = pressure coefficient
- D = hole diameter
- h = convective heat transfer coefficient
- H = impingement gap height
- k = turbulent kinetic energy or thermal conductivity
- L = length
- M = blowing ratio ($\rho_c U_c / \rho_{\infty} U_{\infty}$)
- Ma = Mach number
- Nu = Nusselt number (hD/k_{fluid})
- p = pitch length
- P = pressure
- PS = pressure side streamline
- q = heat flux
- R = thermal resistance (t/k)
- Re = Reynolds number ($\rho_{\infty} U_{\infty} C_{ax} / \mu_{\infty}$)
- s = distance along a streamline starting at $x = 0$
- S = blade span
- SS = suction side streamline

SST= shear stress transport
 t = thickness
 T = temperature
 U = streamwise velocity
 x, y, z = global coordinates, where x is blade axial direction

Greek Symbols

δ_{99} = boundary layer thickness (99%)
 η = adiabatic effectiveness $(T_{\infty} - T_{aw}) / (T_{\infty} - T_{c,exit})$
 θ = momentum thickness
 μ = dynamic viscosity
 ρ = density
 τ = TBC effectiveness $(T_{\infty} - T_{TBC}) / (T_{\infty} - T_{c,in})$
 ϕ = overall effectiveness $(T_{\infty} - T_w) / (T_{\infty} - T_{c,in})$
 ϕ_{TBC} = overall effectiveness under the TBC $(T_{\infty} - T_w) / (T_{\infty} - T_{c,in})$
 χ = internal coolant warming factor for η $(T_{\infty} - T_{c,exit}) / (T_{\infty} - T_{c,in})$

Subscripts, Accents

avg = average
aw = adiabatic wall
c.exit = coolant at film cooling hole exit
c.in = coolant upstream of impingement plate
i = internal
s = static
w = wall or external wall surface
 ∞ = mainstream or external
 $(\bar{\quad})$ = averaged

References

- [1] Padture, N. P., Gell, M., and Jordan, E. H., 2002, "Thermal Barrier Coatings for Gas-Turbine Engine Applications," *Science*, **296**(5566), pp. 280–284.
- [2] Mensch, A., and Thole, K. A., 2014, "Overall Effectiveness of a Blade Endwall With Jet Impingement and Film Cooling," *ASME J. Eng. Gas Turbines Power*, **136**(3), p. 031901.
- [3] Albert, J. E., Bogard, D. G., and Cunha, F., 2004, "Adiabatic and Overall Effectiveness for a Film Cooled Blade," *ASME Paper No. GT2004-53998*.
- [4] Hylton, L. D., Mihelc, M. S., Turner, E. R., Nealy, D. A., and York, R. E., 1983, "Analytical and Experimental Evaluation of the Heat Transfer Distribution Over the Surfaces of Turbine Vanes," NASA Lewis Research Center, Cleveland, OH, Report No. NASA-CR-168015.
- [5] Hylton, L. D., Nirmalan, V., Sultanian, B. K., and Kauffman, R. M., 1988, "The Effects of Leading Edge and Downstream Film Cooling on Turbine Vane Heat Transfer," NASA, Washington, DC, Report No. NASA-CR-182133.
- [6] Turner, E. R., Wilson, M. D., Hylton, L. D., and Kauffman, R. M., 1985, "Turbine Vane External Heat Transfer. Volume 1: Analytical and Experimental Evaluation of Surface Heat Transfer Distributions With Leading Edge Showerhead Film Cooling," NASA Lewis Research Center, Cleveland, OH, Report No. NASA-CR-174827.
- [7] Kang, M. B., and Thole, K. A., 2000, "Flowfield Measurements in the Endwall Region of a Stator Vane," *ASME J. Turbomach.*, **122**(3), pp. 458–466.
- [8] Lynch, S. P., Thole, K. A., Kohli, A., and Lehane, C., 2011, "Computational Predictions of Heat Transfer and Film-Cooling for a Turbine Blade With Non-axisymmetric Endwall Contouring," *ASME J. Turbomach.*, **133**(4), p. 041003.
- [9] Maikell, J., Bogard, D., Piggush, J., and Kohli, A., 2011, "Experimental Simulation of a Film Cooled Turbine Blade Leading Edge Including Thermal Barrier Coating Effects," *ASME J. Turbomach.*, **133**(1), p. 011014.
- [10] Davidson, F. T., Kistenmacher, D. A., and Bogard, D. G., 2014, "Film Cooling With a Thermal Barrier Coating: Round Holes, Craters, and Trenches," *ASME J. Turbomach.*, **136**(4), p. 041007.
- [11] Na, S., Williams, B., Dennis, R. A., Bryden, K. M., and Shih, T. I.-P., 2007, "Internal and Film Cooling of a Flat Plate With Conjugate Heat Transfer," *ASME Paper No. GT2007-27599*.
- [12] Panda, R. K., and Prasad, B. V. S. S., 2012, "Conjugate Heat Transfer From a Flat Plate With Combined Impingement and Film Cooling," *ASME Paper No. GT2012-68830*.
- [13] Dobrowolski, L. D., Bogard, D. G., Piggush, J., and Kohli, A., 2009, "Numerical Simulation of a Simulated Film Cooled Turbine Blade Leading Edge Including Conjugate Heat Transfer Effects," *ASME Paper No. IMECE2009-11670*.
- [14] Ravelli, S., Dobrowolski, L., and Bogard, D. G., 2010, "Evaluating the Effects of Internal Impingement Cooling on a Film Cooled Turbine Blade Leading Edge," *ASME Paper No. GT2010-23002*.
- [15] Mouzon, B. D., Terrell, E. J., Albert, J. E., and Bogard, D. G., 2005, "Net Heat Flux Reduction and Overall Effectiveness for a Turbine Blade Leading Edge," *ASME Paper No. GT2005-69002*.
- [16] Ledezma, G. A., Laskowski, G. M., Dees, J. E., and Bogard, D. G., 2011, "Overall and Adiabatic Effectiveness Values on a Scaled Up Simulated Gas Turbine Vane: Part II—Numerical Simulation," *ASME Paper No. GT2011-46616*.
- [17] Dees, J. E., Bogard, D. G., Ledezma, G. A., and Laskowski, G. M., 2013, "Overall and Adiabatic Effectiveness Values on a Scaled Up, Simulated Gas Turbine Vane," *ASME J. Turbomach.*, **135**(5), p. 051017.
- [18] Dyson, T. E., Bogard, D. G., and Bradshaw, S. D., 2012, "Evaluation of CFD Simulations of Film Cooling Performance on a Turbine Vane Including Conjugate Heat Transfer Effects," *ASME Paper No. GT2012-69107*.
- [19] Williams, R. P., Dyson, T. E., Bogard, D. G., and Bradshaw, S. D., 2014, "Sensitivity of the Overall Effectiveness to Film Cooling and Internal Cooling on a Turbine Vane Suction Side," *ASME J. Turbomach.*, **136**(3), p. 031006.
- [20] Ni, R. H., Humber, W., Fan, G., Johnson, P. D., Downs, J., Clark, J. P., and Koch, P. J., 2011, "Conjugate Heat Transfer Analysis for a Film-Cooled Turbine Vane," *ASME Paper No. GT2011-45920*.
- [21] Ni, R. H., Humber, W., Fan, G., Clark, J. P., Anthony, R. J., and Johnson, J. J., 2013, "Comparison of Predictions From Conjugate Heat Transfer Analysis of a Film-Cooled Turbine Vane to Experimental Data," *ASME Paper No. GT2013-94716*.
- [22] Lynch, S. P., Thole, K. A., Kohli, A., and Lehane, C., 2011, "Heat Transfer for a Turbine Blade With Nonaxisymmetric Endwall Contouring," *ASME J. Turbomach.*, **133**(1), p. 011019.
- [23] Hollworth, B. R., and Dagan, L., 1980, "Arrays of Impinging Jets With Spent Fluid Removal Through Vent Holes on the Target Surface—Part 1: Average Heat Transfer," *ASME J. Eng. Power*, **102**(4), pp. 994–999.
- [24] Kistenmacher, D. A., 2013, "Experimental Investigation of Film Cooling and Thermal Barrier Coatings on a Gas Turbine Vane With Conjugate Heat Transfer Effects," M.S. thesis, University of Texas at Austin, Austin, TX.
- [25] Bunker, R. S., 2009, "The Effects of Manufacturing Tolerances on Gas Turbine Cooling," *ASME J. Turbomach.*, **131**(4), p. 041018.
- [26] Feuerstein, A., Knapp, J., Taylor, T., Ashary, A., Bolcavage, A., and Hitchman, N., 2008, "Technical and Economical Aspects of Current Thermal Barrier Coating Systems for Gas Turbine Engines by Thermal Spray and EBPVD: A Review," *J. Therm. Spray Technol.*, **17**(2), pp. 199–213.
- [27] Soechting, F. O., 1999, "A Design Perspective on Thermal Barrier Coatings," *J. Therm. Spray Technol.*, **8**(4), pp. 505–511.
- [28] Moffat, R. J., 1988, "Describing the Uncertainties in Experimental Results," *Exp. Therm. Fluid Sci.*, **1**(1), pp. 3–17.
- [29] Praisner, T. J., Allen-Bradley, E., Grover, E. A., Knezevici, D. C., and Sjolander, S. A., 2007, "Application of Non-Axisymmetric Endwall Contouring to Conventional and High-Lift Turbine Airfoils," *ASME Paper No. GT2007-27579*.
- [30] Knezevici, D. C., Sjolander, S. A., Praisner, T. J., Allen-Bradley, E., and Grover, E. A., 2010, "Measurements of Secondary Losses in a Turbine Cascade With the Implementation of Nonaxisymmetric Endwall Contouring," *ASME J. Turbomach.*, **132**(1), p. 011013.
- [31] Praisner, T. J., Grover, E. A., Knezevici, D. C., Popovic, I., Sjolander, S. A., Clark, J. P., and Sondergaard, R., 2008, "Toward the Expansion of Low-Pressure-Turbine Airfoil Design Space," *ASME Paper No. GT2008-50898*.
- [32] Lake, J., King, P., and Rivir, R., 1999, "Reduction of Separation Losses on a Turbine Blade With Low Reynolds Numbers," *AIAA Paper No. 99-0242*.
- [33] Murawski, C. G., and Vafai, K., 2000, "An Experimental Investigation of the Effect of Freestream Turbulence on the Wake of a Separated Low-Pressure Turbine Blade at Low Reynolds Numbers," *ASME J. Fluids Eng.*, **122**(2), pp. 431–433.
- [34] Mahallati, A., McAuliffe, B. R., Sjolander, S. A., and Praisner, T. J., 2007, "Aerodynamics of a Low-Pressure Turbine Airfoil at Low-Reynolds Numbers: Part 1—Steady Flow Measurements," *ASME Paper No. GT2007-27347*.
- [35] Zoric, T., Popovic, I., Sjolander, S. A., Praisner, T., and Grover, E., 2007, "Comparative Investigation of Three Highly Loaded LP Turbine Airfoils: Part I—Measured Profile and Secondary Losses at Design Incidence," *ASME Paper No. GT2007-27537*.
- [36] Popovic, I., Zhu, J., Dai, W., Sjolander, S. A., Praisner, T., and Grover, E., 2006, "Aerodynamics of a Family of Three Highly Loaded Low-Pressure Turbine Airfoils: Measured Effects of Reynolds Number and Turbulence Intensity in Steady Flow," *ASME Paper No. GT2006-91271*.
- [37] Lawson, S. A., Lynch, S. P., and Thole, K. A., 2013, "Simulations of Multi-phase Particle Deposition on a Nonaxisymmetric Contoured Endwall With Film-Cooling," *ASME J. Turbomach.*, **135**(3), p. 031032.
- [38] ANSYS, 2010, ANSYS FLUENT, version 13.0.0, ANSYS, Inc., Cannonsburg, PA.
- [39] Menter, F. R., 1994, "Two-Equation Eddy-Viscosity Turbulence Models for Engineering Applications," *AIAA J.*, **32**(8), pp. 1598–1605.
- [40] Schwänen, M., and Duggleby, A., 2009, "Identifying Inefficiencies in Unsteady Pin Fin Heat Transfer," *ASME Paper No. GT2009-60219*.
- [41] Snedden, G., Dunn, D., Ingram, G., and Gregory-Smith, D., 2009, "The Application of Non-Axisymmetric Endwall Contouring in a Single Stage, Rotating Turbine," *ASME Paper No. GT2009-59169*.
- [42] Crawford, M. E., 2009, "TEXSTAN (academic version)," University of Texas, Austin, TX.
- [43] Pointwise, 2013, version 17.1r3, Pointwise, Inc., Fort Worth, TX.
- [44] Marcum, D., and Gaither, J., 1999, "Mixed Element Type Unstructured Grid Generation for Viscous Flow Applications," *AIAA Paper No. 1999-3252*.